TITLE

PDZD8 deficiency drives lipid accumulation in the substantia nigra pars reticulata and disrupts basal ganglia dopaminergic circuits

Running title

Lipid accumulation in SNr disrupts basal ganglia dopaminergic circuits

Authors

Tomoya Ozaki[1†], Yumi Morisugi[1†], Mei Kamino[1†], Hizuki Takahashi[1], Miki Iwata[1], Honoka Maki[1], and Michiko Shirane[1]*

[1]Department of Molecular Biology, Graduate School of Pharmaceutical Sciences, Nagoya City University, Nagoya, Aichi, Japan

***Correspondence**

Michiko Shirane, shiram@phar.nagoya-cu.ac.jp

[†]These authors have contributed equally to this work and share first authorship

Keywords: Brain, Basal ganglia, Dopamine, SNr, Lipid, PDZD8, ADHD

ABSTRACT

The basal ganglia integrate cortical inputs to regulate motor, cognitive, and emotional behaviors through precisely balanced inhibitory and excitatory circuits. The substantia nigra pars reticulata (SNr) functions as a major output nucleus of the basal ganglia, exerting tonic inhibitory control over thalamic and midbrain targets. Although lipid metabolic disturbances have been implicated in neuropsychiatric disorders, how such disturbances affect SNr circuitry and dopaminergic regulation remains poorly understood. Here, we identify a critical role for the lipid transport protein PDZD8 in maintaining basal ganglia circuit integrity. PDZD8 deficiency induces pronounced lipid and lipofuscin accumulation selectively within the SNr. This accumulation is accompanied by enhanced inhibitory inputs from the striatum and reduced SNr projections to the thalamus and midbrain dopaminergic nuclei, indicating a reorganization of inhibitory output pathways. As a consequence, dopaminergic neurons exhibit functional disinhibition and hyperactivation, which in turn reinforces striatal inhibitory signaling, forming a maladaptive feedback loop within the basal ganglia–thalamocortical circuit.

Notably, our previous studies demonstrated that PDZD8$^{-/-}$ mice exhibit hyperactivity, reduced anxiety, impaired fear memory, and increased sensorimotor gating—behavioral features relevant to neurodevelopmental disorders. Together, these findings suggest that lipid accumulation–driven disruption of SNr inhibitory output and dopaminergic regulation may underlie behavioral abnormalities associated with PDZD8 deficiency. Our study highlights PDZD8 as a key regulator of metabolic–circuit coupling in the basal ganglia.

INTRODUCTION

Basal ganglia and striatonigral pathway

The basal ganglia constitute a key component of the volitional motor system and contribute to essential aspects of cognition, sensorimotor integration, emotion, and learning. Dysfunction of basal ganglia circuits is implicated in a wide range of neurological and neuropsychiatric disorders(Park et al., 2020; Foster et al., 2021; McElvain et al., 2021). Current models describe three partially segregated channels of information flow through the basal ganglia—associative, limbic, and sensorimotor—which are further refined into multiple parallel subnetworks(Alexander et al., 1986; Grillner and Robertson, 2016). The cortico–basal ganglia–thalamic network (the basal ganglia–thalamocortical circuitry) represents one of the fundamental network motifs of the brain, consisting of precisely organized and reciprocally connected nodes(Foster et al., 2021; McElvain et al., 2021). Within this loop, the striatum, pallidum, and substantia nigra integrate widespread cortical inputs. The striatonigral (direct) pathway exhibits greater convergence than the striatopallidal (indirect) pathway, yet both ultimately converge onto the same output neurons within the substantia nigra pars reticulata (SNr), emphasizing the integrative nature of SNr-mediated control (Foster et al., 2021).

SNr as a major output nucleus of basal ganglia

SNr is one of the principal output nucleus of the basal ganglia, composed predominantly of inhibitory GABAergic neurons that project to specific thalamic nuclei and brainstem regions(Foster et al., 2021; McElvain et al., 2021; Falasconi et al., 2025). SNr neurons exhibit high tonic firing rates that maintain downstream targets under constant inhibition, whereas transient decreases in firing rate permit movement initiation via disinhibition. Recent studies have revealed that SNr neurons display multiphasic, bidirectional firing dynamics—both decreases and increases—allowing temporally precise modulation of downstream circuits during sequential motor acts(Falasconi et al., 2025). Notably, the caudal and lateral subregions of the SNr, which receive inputs from defined striatal territories, exhibit highly organized topographic projections(Lee et al., 2020; McElvain et al., 2021). These findings suggest that SNr subcircuits play specialized roles in coordinating movement and behavioral control.

SNr dysfunction and neurodevelopmental disorders

Attention-deficit/hyperactivity disorder (ADHD) is characterized by inattention, hyperactivity, and impulsivity, and is linked to altered dopaminergic and noradrenergic signaling(Biederman, 2005; Thapar and Cooper, 2016). Reduced cortical and subcortical gamma-amino butyric acid (GABA) levels have also been reported in ADHD. Among inhibitory neurons, parvalbumin-positive (PV^+) neurons play a key role in attentional

processes and motor control, and their dysfunction has been implicated in multiple psychiatric conditions, including schizophrenia, autism spectrum disorder, and ADHD(Lewis et al., 2005; Sohal et al., 2009). PV^+ neurons in the SNr provide critical feedforward inhibition and disinhibition within basal ganglia circuits. Recent work demonstrated that loss of histamine H_2 receptor (H_2R) expression in SNr PV^+ neurons leads to diminished neuronal activity and behavioral phenotypes resembling ADHD—hyperactivity, impulsivity, and inattention(Kim et al., 2016; Rizzi and Tan, 2019; An et al., 2025). Notably, this dysfunction in SNr PV^+ neurons, but not in medial prefrontal PV^+ neurons, was associated with elevated striatal dopamine levels, implicating the SNr as a key node in the dopaminergic dysregulation underlying ADHD(An et al., 2025). On the other hand, individuals with neurodevelopmental disorders often exhibit symptoms of both ADHD and Autism spectrum disorder (ASD) simultaneously, suggesting underlying common mechanisms in brain development.

Lipid metabolism and neuronal function

Lipid accumulation has long been associated with neurodegenerative conditions such as Alzheimer's disease (AD)(Dahm, 2006; Foley, 2010). The discovery of apolipoprotein E4 (ApoE4) as the strongest genetic risk factor for AD highlighted the importance of lipid metabolism in brain health(Lambert et al., 2013). Abnormal accumulation of cholesteryl esters (CEs)—neutral lipids involved in cholesterol transport—has been observed in brains of AD patients and AD model animals(van der Kant et al., 2019; Nugent et al., 2020; Blanchard et al., 2022; Litvinchuk et al., 2024). ApoE4-containing lipoproteins tend to aggregate within lysosomes, impairing degradation and promoting lipid peroxidation and inflammation. In neurons and glia carrying ApoE4, CEs accumulate in lysosomes and transform into lipofuscin, an autofluorescent granule composed of peroxidized lipids and damaged proteins that is highly resistant to degradation(Guo et al., 2025). Excessive lipofuscin accumulation leads to lysosomal stress and chronic neuroinflammation, processes increasingly recognized as drivers of neurodegeneration(Terman and Brunk, 2004; Gray and Woulfe, 2005; Moreno-Garcia et al., 2018).

PDZD8 and lipid homeostasis in the brain

We previously identified PDZD8 as a tethering protein at intracellular membrane contact sites (MCSs) between the endoplasmic reticulum (ER) and endosomes through proteomic analysis of the protrudin complex(Shirane and Nakayama, 2006; Shirane et al., 2020). PDZD8 belongs to the tubular lipid-binding (TULIP) superfamily and contains a synaptotagmin-like mitochondrial-lipid-binding (SMP) domain that mediates lipid transfer(Elbaz-Alon et al., 2020; Shirane et al., 2020; Gao et al., 2022; Yang et al., 2025). We demonstrated that PDZD8 facilitates cholesterol transport, and that PDZD8-deficient

118 (PDZD8$^{-/-}$) mice exhibit brain-specific accumulation of CEs due to impaired lipophagy—
119 a form of microautophagy in which lipid droplets directly fuse with lysosomes for
120 degradation by lysosomal lipase(Shirane et al., 2020; Morita et al., 2022). In addition, we
121 showed the images with classical ultrastructural features of lipofuscin by transmission
122 electron microscopy (TEM) in PDZD8$^{-/-}$ mouse brains. Behavioral battery analysis
123 revealed that PDZD8$^{-/-}$ mice display pronounced hyperactivity, reduced anxiety and fear,
124 and deficits in fear-conditioned memory and working memory(Kurihara et al., 2023),
125 collectively resembling ADHD-like and ASD-like phenotypes. Moreover, multiple
126 PDZD8 mutations has been linked to human intellectual developmental disorder with
127 autism and dysmorphic facies (IDDADF), a syndromic intellectual disability (ID)
128 accompanied by regional brain hypertrophy and atrophy(Al-Amri et al., 2022; Pantiru et
129 al., 2025).

130 **Present study**

131 Despite these findings, the specific brain regions and neural circuits affected by PDZD8
132 deficiency remained unclear. Here, we demonstrate that PDZD8$^{-/-}$ mice exhibit marked
133 lipid accumulation in the SNr, a major output nucleus of the basal ganglia. This lipid
134 deposition may possibly disrupt the striato–nigro–thalamo–cortical circuitry, leading
135 to disinhibition of dopaminergic neurons and maladaptive reinforcement of striatal
136 inhibitory feedback. These results provide the first evidence that abnormal lipid
137 metabolism in the SNr can remodel basal ganglia circuits, offering new insights into the
138 mechanistic links between lipid dysregulation, dopaminergic imbalance, and ADHD-like
139 and ASD-like behavioral phenotypes.

140

141 **RESULTS**

142 **PDZD8 expression in midbrain neurons and astrocytes**

143 We performed immunostaining using the PDZD8 antibody in PDZD8$^{+/+}$ and PDZD8$^{-/-}$
144 mice to comprehensively analyze the distribution of PDZD8 expression in the brain.
145 Though the specificity of the PDZD8 antibody has been demonstrated in a previous paper
146 (Morita et al., 2022), we compared PDZD8$^{+/+}$ and PDZD8$^{-/-}$ signals in each region and
147 only considered cells with specific signals as PDZD8-expressing cells (Supplementary
148 figure 1A). The results showed that PDZD8 is expressed in multiple regions throughout
149 the brain, but the intensity of expression varied considerably depending on the region and
150 cell type. Brain regions showing notably high expression are shown in Supplementary
151 figure 1B.

152 To determine the cellular distribution of PDZD8, we examined its expression in the
153 midbrain of wild-type mice. PDZD8 was abundantly expressed in SNc, VTA, and SNr,

154 regions defined by dopamine transporter (DAT) expression (Figure 1A). In the SNc and
155 VTA, PDZD8 was localized in DAT- and tyrosine hydroxylase (TH)-positive
156 dopaminergic neurons, respectively (Figure 1B, C). In contrast, PDZD8 was expressed in
157 PV-positive GABAergic neurons and glial fibrillary acidic protein (GFAP)-positive
158 astrocytes within the SNr (Figure 1D, E). Though the SNr is a large region with distinct
159 cellular distributions according to rostral, caudal, medial, and lateral areas, we selected
160 regions for high concordance between PDZD8 and each cell marker. These findings
161 indicate that PDZD8 is highly distributed across neuronal and glial populations around
162 the substantia nigra in midbrain, suggesting its potential role in modulating dopaminergic
163 circuitry.

164 **Marked lipid accumulation in SNr in PDZD8$^{-/-}$ mice**

165 Given that PDZD8$^{-/-}$ mice exhibit abnormal CE accumulation in the brain, we next
166 identified the affected brain regions. LipiDye II staining revealed significant lipid
167 accumulation in several areas, including SNr, dorsal raphe (DR), basolateral amygdala
168 (BLA), and central amygdala (CeA), with the SNr showing the most prominent signal
169 (Figure 2A). Similar results were confirmed in at least three pairs of PDZD8$^{+/+}$ and
170 PDZD8$^{-/-}$ mice, and statistical analysis was performed using images obtained from three
171 mice per genotype. In addition, these results were confirmed by LipiDye II and LipidTOX
172 staining, both of them specifically labels neutral lipids in the hydrophobic core of LDs
173 with a high signal-to-noise ratio (Figure 2B, C). High-resolution Z-stack imaging
174 demonstrated dense intracellular lipid droplets, likely representing lipofuscin, within SNr
175 cells (Figure 2D). Thus, the SNr represents the principal site of lipid deposition in
176 PDZD8$^{-/-}$ mice.

177 **Lipofuscin deposits are enriched in SNr in PDZD8$^{-/-}$ mice**

178 To characterize the lipid deposits in greater detail, serial midbrain sections were stained
179 with LipiDye II and anti-DAT. Large lipid deposits were concentrated in the caudal SNr,
180 while smaller aggregates appeared rostrally (Figure 3A). Ectopic anti-DAT signals were
181 detected in PDZD8$^{-/-}$ SNr, especially in caudal regions, likely overlapping with LipiDye
182 II fluorescence (Figure 3B). Then triple labeling with LipiDye II, DAT, and GFAP in SNr
183 of PDZD8$^{-/-}$ confirmed complete overlap of these signals, consistent with autofluorescent
184 lipofuscin (Figure 3C). These multiple antibodies that should not biologically overlap
185 demonstrated that the observed signals arise from autofluorescent lipofuscin rather than
186 specific immunoreactivity and then most large lipid deposits in the caudal SNr of PDZD8^{-}
187 $^{/-}$ brain are lipofuscin. SNr sections of PDZD8$^{+/+}$ showed no detectable signal in these
188 channels, consistent with the absence of lipofuscin.

189 **Extracellular and intracellular lipid deposits in SNr in PDZD8$^{-/-}$ mice**

Z-stack 3D imaging combined with GFAP staining revealed two types of lipid deposits in the SNr of PDZD8-/- mice: small extracellular deposits, likely lipoproteins, and large intracellular deposits, likely lipofuscin (Figure 4A–C). Extracellular deposits were more abundant medially, while intracellular deposits predominated laterally. 3D reconstructions further distinguished intra- versus extracellular localization (Supplementary movies A, B). Notably, intracellular lipofuscin overlapped with GFAP signals, suggesting autofluorescent properties of astrocytic lipofuscin. However, reliable cell-type identification cannot be achieved based on fluorescence signals alone because of lipofuscin autofluorescence.

Increased striatal projection to SNr in PDZD8$^{-/-}$ mice

To test whether lipid accumulation alters SNr connectivity, we performed retrograde neuronal tracing by injecting Alexa594-CTb into the SNr of PDZD8$^{+/+}$ and PDZD8$^{-/-}$ mice (Figure 5A, B). In both genotypes, injection sites were equivalent. However, corpus striatal (CP) neurons, including pallidum (GP) neurons, projecting to SNr were markedly increased and spatially expanded in PDZD8$^{-/-}$ mice (Figure 5C–E). Similar results were confirmed in at least three pairs of PDZD8$^{+/+}$ and PDZD8$^{-/-}$ mice, and statistical analysis was performed using images obtained from one pair of these mice. In addition, we also observed the similar results with a different mouse pair using the alternative tracer Alexa488-CTb (Supplementary figure 2A–E). These changes indicate enhanced striatal inputs to the SNr (Figure 5F). PDZD8 expression was also detected in dopamine- and cAMP-regulated phosphoprotein (DARPP-32)-positive medium spiny neurons (MSNs) in the striatum (Figure 5G), and DARPP-32 immunoreactivity was significantly elevated in the SNr of PDZD8$^{-/-}$ mice (Figure 5H). Together, these findings suggest strengthened GABAergic striatal inputs to SNr in PDZD8 deficiency.

Decreased projection from SNr in PDZD8$^{-/-}$ mice.

Given that SNr serves as a major output nucleus of the basal ganglia that regulates both thalamic and midbrain dopaminergic neurons, we examined downstream projections by injection of anterograde neuronal tracer palmitoylated GFP (palGFP) into the SNr of PDZD8$^{+/+}$ and PDZD8$^{-/-}$ mice. Injection sites were comparable between groups (Figure 6A, B). In PDZD8$^{-/-}$ mice, projections from the SNr to the VAL/VM and nst (Figure 6C), as well as to the VTA and SNc (Figure 6D), were markedly reduced compared to controls (Figure 6E), indicating disrupted SNr output (Figure 6F). Similar results were confirmed in at least two pairs of PDZD8$^{+/+}$ and PDZD8$^{-/-}$ mice, and statistical analysis was performed using images obtained from one pair of these mice. Although GPi is also a major output nucleus from SNr, palGFP signal in GPi was too faint to determine whether there was a difference between PDZD8$^{+/+}$ and PDZD8$^{-/-}$.

Abnormal dopaminergic circuits in PDZD8$^{-/-}$ mice

Based on these observations, we propose that lipid accumulation in the SNr induces functional disinhibition within the basal ganglia–thalamocortical circuitry (Figure 7). Specifically, lipid deposition in SNr neurons leads to reduced inhibitory output from the SNr to both VAL/VM and the nst, as well as to the VTA and SNc. The consequent disinhibition of thalamic and dopaminergic targets results in hyperactivation of dopaminergic neurons, which in turn enhances inhibitory feedback from striatal GABAergic neurons to SNr, thereby reinforcing the suppression of SNr output. This establishes a maladaptive feedback loop—reduced SNr–thalamic output, dopaminergic disinhibition, and strengthened striatal inhibition—that possibly destabilizes the functional balance of the basal ganglia–thalamocortical circuitry. Such large-scale circuit dysregulation likely underlies the abnormal behavioral phenotypes observed in PDZD8$^{-/-}$ mice, including hyperactivity, reduced anxiety and fear, and impaired fear-memory regulation.

DISCUSSION

Summary of the findings

In this study, we identified a crucial role of the lipid transport protein PDZD8 in maintaining basal ganglia circuit homeostasis. PDZD8 deficiency led to prominent lipid accumulation in the SNr, accompanied by structural and functional remodeling of basal ganglia output pathways. Neuronal tracing analyses revealed reduced SNr projections to both thalamic (VAL/VM, nst) and midbrain dopaminergic targets (VTA, SNc), together with enhanced inhibitory input from striatal GABAergic neurons. These anatomical changes were consistent with functional disinhibition of dopaminergic circuits, resulting in hyperactivation of dopaminergic neurons and maladaptive reinforcement of striatal inhibition. Given that PDZD8$^{-/-}$ mice exhibit hyperactivity and reduced anxiety and fear at the behavioral level—features reminiscent of ADHD-like phenotypes—these findings may possibly establish a direct mechanistic link between lipid metabolic disruption in the SNr, basal ganglia circuit disinhibition, and behavioral dysregulation.

SNr lipid accumulation and circuit disinhibition

The SNr serves as a tonic inhibitory gate in the cortico–basal ganglia–thalamo–cortical loop (basal ganglia–thalamocortical circuit), controlling both motor and cognitive outputs. As a working hypothesis predicted by our data, lipid accumulation within SNr neurons compromises this inhibitory control, likely by affecting cellular excitability and synaptic output. Lipofuscin-like deposits, enriched in cholesteryl esters and peroxidized lipids, are known to induce lysosomal stress, oxidative imbalance, and altered membrane

conductance. These effects may collectively reduce the firing capacity or GABA release efficacy of SNr neurons, thereby reducing inhibitory output to their downstream targets. The observed reduction of SNr projections to VAL/VM and nst implies a loss of inhibitory tone at the thalamic level, which would increase cortical excitability and contribute to hyperactivity. Similarly, decreased inhibition of VTA and SNc dopaminergic neurons produces dopaminergic disinhibition, leading to excessive dopamine release in the striatum. The resulting dopaminergic hyperactivation enhances corticostriatal drive, which strengthens striatal GABAergic feedback to the SNr. This closed-loop maladaptive feedback—SNr hypoactivity, dopaminergic hyperactivation, and enhanced striatal inhibition—creates a self-reinforcing circuit instability. Such loop-level dysregulation likely underlies the behavioral abnormalities observed in PDZD8$^{-/-}$ mice.

Disinhibition-driven distortion of RPE signaling in the VTA–BLA circuit

Beyond basal ganglia output pathways, the disinhibition of dopaminergic neurons observed in PDZD8$^{-/-}$ mice likely extends its impact to broader reward-related networks, particularly the VTA–BLA circuit, which encodes reward prediction error (RPE) signals during associative learning. The VTA conveys phasic dopamine release to the BLA during both appetitive and aversive conditioning, where dopaminergic modulation shapes the associative strength between conditioned and unconditioned stimuli. Disruption of inhibitory control from the SNr to midbrain dopaminergic neurons may bias RPE computation—amplifying positive prediction signals while diminishing aversive or omission-related responses. Such imbalance could account for the hyperactivity and impaired fear memory observed in PDZD8$^{-/-}$ mice, reflecting aberrant valuation of outcomes and a failure to encode negative prediction errors. In this framework, lipid accumulation–induced disinhibition of the SNr may distort dopaminergic gain control within the VTA–BLA network, leading to maladaptive reinforcement learning and emotional dysregulation. This suggests that PDZD8-dependent lipid homeostasis in the SNr is essential for maintaining the dynamic balance between positive and negative RPE signaling across cortico–amygdalo–dopaminergic loops.

Comparison with prior studies on basal ganglia and ADHD

Our findings extend previous evidence implicating SNr dysfunction in the pathophysiology of ADHD. Earlier studies demonstrated that H_2R deficiency in PV^+ neurons of the SNr reduces inhibitory output and induces hyperactivity and impulsivity. Similarly, reduced GABAergic tone and enhanced dopaminergic transmission have been reported in ADHD patients and model animals. The present work suggests that lipid metabolic stress may represent a previously unrecognized upstream mechanism producing a similar disinhibitory outcome. PDZD8 is an ER–endosome tethering protein

required for lipid transport and membrane contact site integrity. Loss of PDZD8 impairs lipophagy, leading to intracellular lipid droplet accumulation and lipofuscin formation. These pathological deposits are not inert: they alter calcium handling, disrupt mitochondrial dynamics, and perturb synaptic vesicle turnover. The convergence of lysosomal and GABAergic dysfunction in SNr neurons likely explains the observed circuit-level changes. Therefore, disinhibition of SNr neurons emerges as a new paradigm linking lipid homeostasis to dopaminergic regulation and behavioral control. However, areas beyond those shown in this study may also be involved in ADHD-like behavior of PDZD8$^{-/-}$. While lipid accumulation in PDZD8$^{-/-}$ is most pronounced in SNr, significant lipid accumulation is also observed in DR, BLA, and CeA (Figure 2A). Therefore, future studies should investigate abnormalities in regions beyond SNr. ADHD is primarily considered a dysfunction of circuits connecting PFC and basal ganglia, which govern attention and executive function, with dopamine and noradrenaline involved in controlling these circuits. Furthermore, amygdala, which regulates emotions, and raphe nuclei, which control impulsivity, are also implicated in ADHD, with serotonin involved in regulation of these circuits. It is necessary to investigate abnormalities in these circuits and neurotransmitters in PDZD8$^{-/-}$ mice.

Regulation of inhibitory circuits by lipid metabolism

Although direct evidence for lipid deposition within neurons in PDZD8$^{-/-}$ has not been obtained, the morphology and size of lipid-accumulating cells in PDZD8$^{-/-}$ mice suggest they must be neurons. For example, in Figure 4C (LipiDyeII+GFAP), the two central white cells exhibit the characteristic pyramidal shape of neurons, with a cell body diameter exceeding 10 μm, significantly larger than the size of astrocyte cell bodies, which have a diameter of 5 μm or less. Similarly, in Figure 2D (LipiDyeII+DIC), lipid-accumulating cells in PDZD8$^{-/-}$ also exhibit the morphology and size of pyramidal cells thought to be neurons. Lipid homeostasis is increasingly recognized as a determinant of neuronal function. Our findings highlight that inhibitory GABAergic circuits are particularly sensitive to metabolic stress. The SNr, characterized by high tonic firing rates, may be especially vulnerable to disruptions in lipid trafficking and degradation. Accumulation of peroxidized lipids and lipofuscin can impair GABA release machinery and ion channel stability, thereby compromising tonic inhibition. Astrocytic PDZD8 expression observed in our study suggests that glia–neuron lipid coupling may be essential for maintaining SNr function. Disruption of such glial lipid buffering could amplify local oxidative stress and propagate dysfunction across the basal ganglia network.

Implications for neuropsychiatric and neurodegenerative disorders

The link between lipid accumulation and circuit disinhibition identified here may have

broader implications beyond ADHD. Lipofuscin accumulation and lysosomal dysfunction are hallmarks of Alzheimer's disease and aging-related cognitive decline. The present findings suggest that even in the absence of overt neurodegeneration, lipid metabolic perturbations can remodel inhibitory circuits and alter behavioral state. Given the prominent dopaminergic involvement, PDZD8 dysfunction may represent a shared vulnerability factor bridging metabolic stress, dopamine dysregulation, and cognitive-behavioral disorders related to basal ganglia or SNr.

Limitation of the study

Because lipofuscin exhibits strong autofluorescence, it remains unproven whether the lipid-accumulating cells observed in PDZD8$^{-/-}$ mice are neurons. Although immunostaining using wavelength-specific filters to visualize lipofuscin has been reported(Guo et al., 2025), we were unable to establish this method in the present study. Also, cell-type assignment based solely on fluorescence is not possible due to lipofuscin autofluorescence.

Especially, the regional specificity of lipofuscin accumulation in the SNr remains unexplained and is an important topic for future investigation

While quantitative analysis of the entire SNr region was performed (Figure 2A), quantitative analyses across serial sections (Figure 3) and three-dimensional reconstructions (Figure 4) will be important in future studies.

The causal relationship and mechanisms linking lipid accumulation to circuit reorganization in PDZD8$^{-/-}$ mice remain unresolved. However, previous studies have shown that excessive lipofuscin accumulation induces lipid peroxidation–mediated reactive oxygen species production, leading to lysosomal stress and chronic neuroinflammation that promote neurodegeneration(Terman and Brunk, 2004; Gray and Woulfe, 2005; Moreno-Garcia et al., 2018; Guo et al., 2025). Future studies should directly quantify intracellular lipid peroxides and reactive oxygen species to test this hypothesis.

Direct measurements of dopamine and its metabolites would provide important insight but are technically challenging and were not feasible in the present study.

Although PDZD8 is broadly expressed throughout the brain, lipid accumulation was selectively prominent in the SNr of PDZD8$^{-/-}$ mice. The basis of this regional vulnerability remains unclear and warrants further investigation, including potential contributions of PDZD8-interacting complex components. Future studies combining in vivo dopamine imaging, electrophysiological recordings of SNr neurons, and cell-type–specific PDZD8 rescue approaches will be required to define the relative contributions of neuronal and glial populations. In addition, pharmacological or genetic restoration of lipid

370 homeostasis may help determine whether normalization of lipid metabolism can rescue
371 basal ganglia circuit stability and associated behavioral deficits.

372 **Conclusion**

373 Together, our findings reveal that PDZD8-dependent lipid metabolism is indispensable
374 for preserving inhibitory control within the basal ganglia and ensuring accurate
375 dopaminergic prediction error signaling, providing a unifying mechanistic framework
376 linking metabolic stress, circuit disinhibition, and behavioral dysregulation.

377

378 **METHODS**

379 **Animals**

380 Mice were housed under 12-h light/dark cycle with food and water ad libitum. All
381 mouse experiments were approved by the animal ethics committee of Nagoya City
382 University. All experiments were performed using at least two sets of paired mice
383 (PDZD8$^{+/+}$ and PDZD8$^{-/-}$). Mouse sex and age were matched across experiments, and
384 both mice in each pair were analyzed simultaneously. In all experiments, mice were
385 aged 4–9 months and were either male or female. Figures show representative images
386 from one of the multiple experiments performed. A summary table listing these mouse
387 details is shown in Supplementary table 1.

388 **Mutant mice**

389 Generation of PDZD8-KO mice was described previously(Morita et al., 2022). In brief,
390 Cas9 nickase mRNA, Generic tracrRNA, and target-specific crRNA were mixed and
391 injected into C57BL/6J mouse zygotes. The resultant mutant mice were backcrossed
392 with C57BL/6J mice before experiments. Animals were genotyped by PCR analysis.

393 **Antibodies and reagents**

394 Rabbit polyclonal antibodies to PDZD8 were from Sigma-Aldrich; mouse monoclonal
395 antibodies to TH were from Sigma-Aldrich; mouse monoclonal antibodies to GFAP
396 were from Proteintech; guinea pig polyclonal antibodies to DAT, PV, and DARPP were
397 from Frontier institute; Alexa Fluor 488 goat anti-rabbit IgG, Alexa Fluor 555 goat anti-
398 mouse IgG, Alexa Fluor 555 goat anti-guinea pig IgG, Alexa Fluor 647 goat anti-guinea
399 pig IgG, Alexa Fluor 488 cholera toxin B, Alexa Fluor 594 cholera toxin B, and
400 LipidTox were from Thermo Fisher Scientific; LipiDye II was from Funakoshi.

401 **Immunohistofluorescence analysis**

402 Mouse brain was fixed with 2% paraformaldehyde in phosphate-buffered saline (PBS,
403 Wako), exposed consecutively to 15% and 30% sucrose in PBS for 2 days, and
404 embedded in tissue-Tek OCT compound (SAKURA). Thin sections were prepared with
405 a cryostat microtome (CM1850 UV, Leica) and stained consecutively with primary

antibodies and Alexa Fluor–labeled secondary antibodies in PBS containing 0.5% Triton X-100, or stained with LipiDye II or LipidTox in PBS. The sections were observed with an LSM800 confocal microscope (Zeiss), and the images were processed for calculation of fluorescence intensity with ZEN imaging software (Zeiss). Brain regions were referenced from Allen Brain Atlas (http://atlas.brain-map.org).

Stereotaxic injection

Mice were anesthetized intraperitoneally with a mixture of midazolam (4 mg kg^{-1}, SANDOZ, Tokyo, Japan), medetomidine (0.75 mg kg^{-1}, Kyoritsu Seiyaku, Tokyo, Japan) and butorphanol (5 mg kg^{-1}, Meiji Seika Pharma, Tokyo, Japan) and placed in a stereotaxic frame (NARISHIGE, Tokyo, Japan). Body temperature was maintained at 37 °C. The scalp was sterilized and incised, and a small craniotomy was made above the target. Alexa Fluor 594– or 488–conjugated cholera toxin subunit B (CTb, Thermo Fisher Scientific, MA, USA) was prepared at 2 μg μL^{-1} in sterile PBS. AAV2-CMV-palGFP virus particles were from Dr. Nakamura(Yahiro et al., 2023). 200 nl of Alexa Fluor 594-CTb was injected into the SNr (coordinates from Bregma: AP: -3.2 mm, ML: ±1.4 mm, DV: -4.4 mm). 150 nl of Alexa Fluor 488-CTb was injected into the SNr (coordinates from Bregma: AP: -3.7 mm, ML: ±1.8 mm, DV: -4.5 mm). 100 nl of AAV solution was injected into the SNr (coordinates from Bregma: AP: -3.7 mm, ML: ±1.8 mm, DV: -4.5 mm). Tracer (200 nL per site) was delivered using a Hamilton microsyringe (1701RN Neuros Syringe, 33G; Hamilton Company, NV, USA) connected to a motorized stereotaxic microinjector (NARISHIGE, Tokyo, Japan ; 100 nL min^{-1}). After infusion, the needle was left in place for 10–15 min to minimize reflux before being withdrawn slowly. For each mouse, injections were made at the following stereotaxic coordinates relative to bregma: [AP -3.2], [ML ±1.4], [DV -4.4] (mm). The scalp was closed with sutures, and mice were monitored until full recovery. After surgery, mice received postoperative care including an intraperitoneal injection of antibiotic (amoxicillin, Kyoritsu Seiyaku, Tokyo, Japan; 50 mg kg^{-1}, i.p.). Information of tracer injection was summarized in Supplementary table 2.

Histological analysis of neural tracing

Mouse brain was fixed with 2% paraformaldehyde in PBS, exposed consecutively to 15% and 30% sucrose in PBS for 2 days, and embedded in OCT compound. Thin sections (50 μm) were prepared with a cryostat microtome. The sections were observed with an LSM800 confocal microscope. The distribution of the tracer at the injection site was verified, and only sections without substantial displacement of the injection site were included in the analysis. The sections were imaged using a LSM800 to acquire fluorescence images. The images were processed for calculation of fluorescence intensity

with ZEN imaging software. Regions of interest (ROIs) were defined on the acquired images, and fluorescence intensity values were extracted. Background fluorescence was subtracted to obtain tracer-specific signal intensities. Tracer signals were quantified for both the injection sites and the target regions, and values from the target regions were normalized to those of the corresponding injection sites.

Statistical analysis

For lipid imaging, statistical analysis was performed with the use of BellCurve for Excel software (Social Survey Research Information, Tokyo, Japan). Normality of data was assessed with the Shapiro-Wilk test. If the normality was not met, the Mann-Whitney U test was applied (Fig. 2A, SNr; DR; BLA). If data were normally distributed and variance was homogeneous between genotypes, comparisons were performed with Student's *t* test. If homogeneity of variance was not assumed, Welch's *t* test was applied instead of Student's *t* test (Fig. 2A, CeA). For neuronal tracing, statistical analysis was performed using Microsoft Excel. Variance homogeneity was assessed using an F-test, and based on the results, appropriate t-tests, Welch's t test (Fig. 6E, VAL/VM; SNc) or Student's t test (Fig. 5E, Str; Fig. 6E, VTA; SNc) were applied to evaluate statistical significance. Quantitative data are presented as mean ± SE. Statistical significance of a *P* value is indicated as $p < 0.05$ (*) and $p < 0.001$ (***). Sample size (*n*) are in the figure legends.

Acknowledgements

We thank K. Nakamura for AAV2-CMV-palGFP virus particles, I. Yamahata for Immunofluorescent analysis, N. Takahashi for discussion, and the Research Equipment Sharing Center at Nagoya City University for assistance.

Author contributions statement

M.S. conceptualized and supervised the study, acquired funding, designed experiments, and wrote the manuscript; T.O., Y.M., M.K., and H.T. performed experiments; M.I. and H.M. prepared resources.

Funding information

This work was supported in part by KAKENHI grants from Japan Society for the Promotion of Science (JSPS) to M.S. (24K02122).

Ethics

The animal study was approved by Nagoya City University, Animal Research

Committee. The study was conducted in accordance with the local legislation and institutional requirements.

Data availability and sources

The original contributions presented in the study are included in the article/ supplementary material, further inquiries can be directed to the corresponding author.

REFERENCES

Al-Amri, A.H., Armstrong, P., Amici, M., Ligneul, C., Rouse, J., El-Asrag, M.E., et al. (2022). PDZD8 Disruption Causes Cognitive Impairment in Humans, Mice, and Fruit Flies. *Biol Psychiatry* 92(4)**,** 323-334. doi: 10.1016/j.biopsych.2021.12.017.

Alexander, G.E., DeLong, M.R., and Strick, P.L. (1986). Parallel organization of functionally segregated circuits linking basal ganglia and cortex. *Annu Rev Neurosci* 9**,** 357-381. doi: 10.1146/annurev.ne.09.030186.002041.

An, D., You, Y., Ma, Q., Xu, Z., Liu, Z., Liao, R., et al. (2025). Deficiency of histamine H(2) receptors in parvalbumin-positive neurons leads to hyperactivity, impulsivity, and impaired attention. *Neuron* 113(4)**,** 572-589 e576. doi: 10.1016/j.neuron.2024.12.002.

Biederman, J. (2005). Attention-deficit/hyperactivity disorder: a selective overview. *Biol Psychiatry* 57(11)**,** 1215-1220. doi: 10.1016/j.biopsych.2004.10.020.

Blanchard, J.W., Akay, L.A., Davila-Velderrain, J., von Maydell, D., Mathys, H., Davidson, S.M., et al. (2022). APOE4 impairs myelination via cholesterol dysregulation in oligodendrocytes. *Nature* 611(7937)**,** 769-779. doi: 10.1038/s41586-022-05439-w.

Dahm, R. (2006). Alzheimer's discovery. *Curr Biol* 16(21)**,** R906-910. doi: 10.1016/j.cub.2006.09.056.

Elbaz-Alon, Y., Guo, Y., Segev, N., Harel, M., Quinnell, D.E., Geiger, T., et al. (2020). PDZD8 interacts with Protrudin and Rab7 at ER-late endosome membrane contact sites associated with mitochondria. *Nat Commun* 11(1)**,** 3645. doi: 10.1038/s41467-020-17451-7.

Falasconi, A., Kanodia, H., and Arber, S. (2025). Dynamic basal ganglia output signals license and suppress forelimb movements. *Nature* 644(8077)**,** 749-758. doi: 10.1038/s41586-025-09066-z.

Foley, P. (2010). Lipids in Alzheimer's disease: A century-old story. *Biochim Biophys Acta* 1801(8)**,** 750-753. doi: 10.1016/j.bbalip.2010.05.004.

Foster, N.N., Barry, J., Korobkova, L., Garcia, L., Gao, L., Becerra, M., et al. (2021). The

514 mouse cortico-basal ganglia-thalamic network. *Nature* 598(7879), 188-194. doi:
515 10.1038/s41586-021-03993-3.
516 Gao, Y., Xiong, J., Chu, Q.Z., and Ji, W.K. (2022). PDZD8-mediated lipid transfer at
517 contacts between the ER and late endosomes/lysosomes is required for neurite
518 outgrowth. *J Cell Sci* 135(5). doi: 10.1242/jcs.255026.
519 Gray, D.A., and Woulfe, J. (2005). Lipofuscin and aging: a matter of toxic waste. *Sci*
520 *Aging Knowledge Environ* 2005(5), re1. doi: 10.1126/sageke.2005.5.re1.
521 Grillner, S., and Robertson, B. (2016). The Basal Ganglia Over 500 Million Years. *Curr*
522 *Biol* 26(20), R1088-R1100. doi: 10.1016/j.cub.2016.06.041.
523 Guo, J.L., Braun, D., Fitzgerald, G.A., Hsieh, Y.T., Rouge, L., Litvinchuk, A., et al. (2025).
524 Decreased lipidated ApoE-receptor interactions confer protection against
525 pathogenicity of ApoE and its lipid cargoes in lysosomes. *Cell* 188(1), 187-206
526 e126. doi: 10.1016/j.cell.2024.10.027.
527 Kim, H., Ahrlund-Richter, S., Wang, X., Deisseroth, K., and Carlen, M. (2016). Prefrontal
528 Parvalbumin Neurons in Control of Attention. *Cell* 164(1-2), 208-218. doi:
529 10.1016/j.cell.2015.11.038.
530 Kurihara, Y., Mitsunari, K., Mukae, N., Shoji, H., Miyakawa, T., and Shirane, M. (2023).
531 PDZD8-deficient mice manifest behavioral abnormalities related to emotion,
532 cognition, and adaptation due to dyslipidemia in the brain. *Mol Brain* 16(1), 11.
533 doi: 10.1186/s13041-023-01002-4.
534 Lambert, J.C., Ibrahim-Verbaas, C.A., Harold, D., Naj, A.C., Sims, R., Bellenguez, C., et
535 al. (2013). Meta-analysis of 74,046 individuals identifies 11 new susceptibility
536 loci for Alzheimer's disease. *Nat Genet* 45(12), 1452-1458. doi: 10.1038/ng.2802.
537 Lee, J., Wang, W., and Sabatini, B.L. (2020). Anatomically segregated basal ganglia
538 pathways allow parallel behavioral modulation. *Nat Neurosci* 23(11), 1388-1398.
539 doi: 10.1038/s41593-020-00712-5.
540 Lewis, D.A., Hashimoto, T., and Volk, D.W. (2005). Cortical inhibitory neurons and
541 schizophrenia. *Nat Rev Neurosci* 6(4), 312-324. doi: 10.1038/nrn1648.
542 Litvinchuk, A., Suh, J.H., Guo, J.L., Lin, K., Davis, S.S., Bien-Ly, N., et al. (2024).
543 Amelioration of Tau and ApoE4-linked glial lipid accumulation and
544 neurodegeneration with an LXR agonist. *Neuron* 112(3), 384-403 e388. doi:
545 10.1016/j.neuron.2023.10.023.
546 McElvain, L.E., Chen, Y., Moore, J.D., Brigidi, G.S., Bloodgood, B.L., Lim, B.K., et al.
547 (2021). Specific populations of basal ganglia output neurons target distinct brain
548 stem areas while collateralizing throughout the diencephalon. *Neuron* 109(10),
549 1721-1738 e1724. doi: 10.1016/j.neuron.2021.03.017.

550 Moreno-Garcia, A., Kun, A., Calero, O., Medina, M., and Calero, M. (2018). An
551 Overview of the Role of Lipofuscin in Age-Related Neurodegeneration. *Front*
552 *Neurosci* 12**,** 464. doi: 10.3389/fnins.2018.00464.
553 Morita, K., Wada, M., Nakatani, K., Matsumoto, Y., Hayashi, N., Yamahata, I., et al.
554 (2022). PDZD8-deficient mice accumulate cholesteryl esters in the brain as a
555 result of impaired lipophagy. *iScience* 25(12)**,** 105612. doi:
556 10.1016/j.isci.2022.105612.
557 Nugent, A.A., Lin, K., van Lengerich, B., Lianoglou, S., Przybyla, L., Davis, S.S., et al.
558 (2020). TREM2 Regulates Microglial Cholesterol Metabolism upon Chronic
559 Phagocytic Challenge. *Neuron* 105(5)**,** 837-854 e839. doi:
560 10.1016/j.neuron.2019.12.007.
561 Pantiru, A.D., Van de Sompele, S., Ligneul, C., Chatelain, C., Barrea, C., Lerch, J.P., et
562 al. (2025). Autistic behavior is a common outcome of biallelic disruption of
563 PDZD8 in humans and mice. *Mol Autism* 16(1)**,** 14. doi: 10.1186/s13229-025-
564 00650-8.
565 Park, J., Coddington, L.T., and Dudman, J.T. (2020). Basal Ganglia Circuits for Action
566 Specification. *Annu Rev Neurosci* 43**,** 485-507. doi: 10.1146/annurev-neuro-
567 070918-050452.
568 Rizzi, G., and Tan, K.R. (2019). Synergistic Nigral Output Pathways Shape Movement.
569 *Cell Rep* 27(7)**,** 2184-2198 e2184. doi: 10.1016/j.celrep.2019.04.068.
570 Shirane, M., and Nakayama, K.I. (2006). Protrudin induces neurite formation by
571 directional membrane trafficking. *Science* 314(5800)**,** 818-821. doi:
572 10.1126/science.1134027.
573 Shirane, M., Wada, M., Morita, K., Hayashi, N., Kunimatsu, R., Matsumoto, Y., et al.
574 (2020). Protrudin and PDZD8 contribute to neuronal integrity by promoting lipid
575 extraction required for endosome maturation. *Nat Commun* 11(1)**,** 4576. doi:
576 10.1038/s41467-020-18413-9.
577 Sohal, V.S., Zhang, F., Yizhar, O., and Deisseroth, K. (2009). Parvalbumin neurons and
578 gamma rhythms enhance cortical circuit performance. *Nature* 459(7247)**,** 698-702.
579 doi: 10.1038/nature07991.
580 Terman, A., and Brunk, U.T. (2004). Lipofuscin. *Int J Biochem Cell Biol* 36(8)**,** 1400-
581 1404. doi: 10.1016/j.biocel.2003.08.009.
582 Thapar, A., and Cooper, M. (2016). Attention deficit hyperactivity disorder. *Lancet*
583 387(10024)**,** 1240-1250. doi: 10.1016/S0140-6736(15)00238-X.
584 van der Kant, R., Langness, V.F., Herrera, C.M., Williams, D.A., Fong, L.K., Leestemaker,
585 Y., et al. (2019). Cholesterol Metabolism Is a Druggable Axis that Independently

586 Regulates Tau and Amyloid-beta in iPSC-Derived Alzheimer's Disease Neurons.
587 *Cell Stem Cell* 24(3), 363-375 e369. doi: 10.1016/j.stem.2018.12.013.
588 Yahiro, T., Kataoka, N., and Nakamura, K. (2023). Two Ascending Thermosensory
589 Pathways from the Lateral Parabrachial Nucleus That Mediate Behavioral and
590 Autonomous Thermoregulation. *J Neurosci* 43(28), 5221-5240. doi:
591 10.1523/JNEUROSCI.0643-23.2023.
592 Yang, H., Xun, J., Li, Y., Mondal, A., Lv, B., Watkins, S.C., et al. (2025). LYVAC/PDZD8
593 is a lysosomal vacuolator. *Science* 389(6762), eadz0972. doi:
594 10.1126/science.adz0972.
595
596

FIGURE LEGENDS

Figure 1. PDZD8 is highly expressed in neurons and astrocytes in the midbrain.
Immunofluorescence analysis of wild-type mouse brain.
(A) Dopamine transporter (DAT, magenta) and PDZD8 (green) in the midbrain. Regions corresponding to substantia nigra pars compacta (SNc), ventral tegmental area (VTA), and substantia nigra pars reticulata (SNr) are indicated in the DAT image. The merged image is also shown. Scale bars, 200 μm.
(B) PDZD8 (green) and DAT (magenta) in SNc.
(C) PDZD8 (green) and tyrosine hydroxylase (TH, magenta) in VTA.
(D) PDZD8 (green) and parvalbumin (PV, magenta) in SNr.
(E) PDZD8 (green) and GFAP (magenta) in SNr. Scale bars, 20 μm (B–E).

Figure 2. Lipofuscin deposits are markedly increased in SNr in PDZD8$^{-/-}$ mice.
Lipid aggregate analysis of PDZD8$^{+/+}$ and PDZD8$^{-/-}$ mouse brains.
(A) Dot plots showing mean fluorescence intensity of LipiDye II in SNr, dorsal raphe (DR), basolateral amygdala (BLA), and central amygdala (CeA). Schematic brain sections indicate the regions analyzed. Red lines in sagittal sections (upper) indicate the positions of coronal sections (lower), and red boxes mark the analyzed regions. Sample size (*n*) denotes the number of images from three mice per each genotype.
(B, C) Confocal images of LipiDye II (B) and LipidTox (C) in SNr. Boxed regions (left) are shown at higher magnification (right). Scale bars, 50 μm (left) and 20 μm (right).
(D) High-resolution images of LipiDye II in SNr of PDZD8$^{-/-}$ mice. Boxed regions (left) are shown enlarged (right). A differential interference contrast (DIC) image is also shown. The dotted line outlines a cell periphery densely packed with lipofuscin (right). Scale bars, 5 μm.

Figure 3. Lipofuscin deposits are enriched in SNr in PDZD8$^{-/-}$ mice.
Lipid aggregate analysis of SNr in PDZD8$^{+/+}$ and PDZD8$^{-/-}$ mouse brains.
(A) Confocal images of DAT (magenta) and LipiDye II (green) in serial sections of SNr from rostral (left) to caudal (right) regions at 240 μm intervals. Scale bars, 100 μm. For PDZD8-/-, enlarged images of LipiDye II are also shown. Scale bars, 20 μm.
(B) The merged images of DAT and DIC for the images outlined in (A) in PDZD8$^{+/+}$ and PDZD8$^{-/-}$. The merged images of LipiDye II and DIC in PDZD8$^{-/-}$ are also shown. The region of ectopic DAT signal is outlined with a dotted line. Scale bars, 100 μm.
(C) Confocal images of LipiDye II (green), DAT (blue), and GFAP (magenta) in SNr in PDZD8$^{-/-}$. The merged image is also shown. Scale bars, 20 μm.

633

634 **Figure 4. Extracellular and intracellular lipid deposits in SNr in PDZD8-/- mice.**
635 (A) Scheme of coronal section containing SNr from mouse brain atlas (left), in which
636 SNr is shown enlarged (right) with the medial (M) and lateral (L) regions indicated.
637 (B, C) 3D images of LipiDye II (green) and GFAP (magenta) in medial (B) and lateral
638 (C) regions of SNr in PDZD8$^{-/-}$ mice, which are reconstructed from z-stack confocal
639 images using Imaris software. Scale bars, 10 μm.
640

641 **Figure 5. Abnormal striatal projection to SNr in PDZD8$^{-/-}$ mice.**
642 (A, B) Confocal images of Alexa594-conjugated cholera toxin subunit B (Alexa594-
643 CTb) injected to SNr merged with DIC images. Tiling images of cerebral hemisphere
644 (A) and serial sections from rostral (left) to caudal (right) regions at 50 μm intervals
645 focusing on SNr (B). Scale bars, 500 μm (A) and 200 μm (B).
646 (C, D) Confocal images of Alexa594-CTb merged with DIC images of brain region
647 containing striatum, indicating projection sources. Tiling images of cerebral hemisphere
648 (C) and serial sections from rostral (left) to caudal (right) regions at 50 μm intervals
649 focusing on striatum (D). Scale bars, 500 μm (C) and 200 μm (D).
650 (E) Dot plots showing normalized ratio of mean fluorescence intensity of Alexa594-
651 CTb at Str (striatum). Sample size (*n*) denotes the number of images per mouse.
652 (F) Schematic representation of striatal projections to SNr, with showing increase in
653 PDZD8$^{-/-}$ mice compared to PDZD8$^{+/+}$ mice. Injection sites of Alexa594-CTb to SNr are
654 also indicated.
655 (G) Immunofluorescence images of PDZD8 (green) and dopamine- and cAMP-
656 regulated phosphoprotein (DARPP-32, magenta) in striatum of wild-type mice, with
657 merged image. Scale bars, 20 μm.
658 (H) Immunofluorescence images of DARPP and merged with DIC in SNr of PDZD8$^{+/+}$
659 and PDZD8$^{-/-}$. Scale bars, 100 μm.
660

661 **Figure 6. Abnormal projection from SNr in PDZD8$^{-/-}$ mice.**
662 (A, B) Confocal images showing palmitoylated GFP (palGFP) injection sites in SNr
663 merged with DIC images. Tiling images of cerebral hemisphere (A) and serial sections
664 from rostral (left) to caudal (right) regions at 100 μm intervals focusing on SNr (B).
665 Scale bars, 500 μm (A); 200 μm (B).
666 (C) Confocal and merged DIC images of thalamic regions showing SNr projection
667 targets. PalGFP signals indicate SNr projections to the ventral anterior-lateral complex

of the thalamus (VAL), ventromedial thalamus (VM), and the nigrostriatal tract (nst). Scale bars, 200 μm.

(D) Confocal and merged DIC images of midbrain regions showing SNr projections to the ventral tegmental area (VTA) and substantia nigra pars compacta (SNc). Scale bars, 200 μm.

(E) Dot plots showing normalized ratio of mean fluorescence intensity of palGFP at VAL/VM, nst, VTA, and SNc. Sample size (*n*) denotes the number of images per mouse.

(F) Schematic illustration summarizing the anterograde tracing results. Projections from the SNr to both VM/nst and VTA/SNc are markedly reduced in PDZD8$^{-/-}$ mice compared with PDZD8$^{+/+}$ mice. Injection sites of palGFP in the SNr are indicated.

Figure 7. Abnormal dopaminergic circuits in PDZD8$^{-/-}$ mice.

Proposed circuit model depicting the consequences of lipid accumulation in the SNr of PDZD8$^{-/-}$ mice. In PDZD8$^{+/+}$ mice (left), striatal GABAergic inputs transiently inhibit SNr neurons, which tonically suppress activity in thalamic (VM/nst) and midbrain dopaminergic (VTA/SNc) targets, maintaining balanced inhibitory control within the basal ganglia–thalamocortical circuit. In PDZD8$^{-/-}$ mice (right), lipid accumulation in SNr neurons reduces their inhibitory output to VM/nst and VTA/SNc, resulting in functional disinhibition of thalamic and dopaminergic pathways. The consequent hyperactivation of dopaminergic neurons increases dopamine release in the striatum, thereby enhancing inhibitory feedback from striatal neurons to the SNr. This establishes a maladaptive feedback loop—reduced SNr–thalamic output, dopaminergic hyperactivation, and strengthened striatal inhibition—that destabilizes the functional balance of the basal ganglia–thalamocortical circuit and underlies the ADHD-like behavioral abnormalities observed in PDZD8$^{-/-}$ mice.

SUPPLEMENTARY FIGURE LEGENDS

Supplementary figure 1. Specificity of anti-PDZD8 antibody.

(A) Immunofluorescence analysis of PDZD8$^{+/+}$ and PDZD8$^{-/-}$ mice. PDZD8 (green) and the merged image of PDZD8 (green), DAT (red), and Hoechst (blue) in the VTA region are shown. Scale bars, 10 μm.

(B) The summary of brain regions and cell types whether they were colocalized or not with PDZD8. Immunostaining with the anti-PDZD8 antibody in PDZD8$^{+/+}$ and PDZD8$^{-/-}$ mice were comprehensively analyzed. (+) indicates "colocalization of PDZD8

703 and cell marker"; (-) indicates "no colocalization of PDZD8 and cell marker"; nt
704 indicates "not tested."
705
706 **Supplementary figure 2. Autofluorescence of lipofuscin at SNr in PDZD8$^{-/-}$ mice.**
707 Confocal fluorescent images and merged DIC images of unstained slices of SNr in
708 PDZD8$^{+/+}$ and PDZD8$^{-/-}$ mouse brains. Fluorescence was observed with GFP channel.
709 Scale bars, 20 μm.
710
711 **Supplementary figure 3. Increased striatal projection to SNr in PDZD8$^{-/-}$ mice.**
712 (A, B) Confocal images of Alexa488-CTb injected to SNr merged with DIC images.
713 Tiling images of cerebral hemisphere (A) and images focused on SNr (B). Scale bars,
714 500 μm (A) and 200 μm (B).
715 (C, D) Confocal images of Alexa488-CTb merged with DIC images of brain region
716 containing Str (striatum), indicating projection sources. Tiling images of cerebral
717 hemisphere (C) and images focused on striatum (D). Scale bars, 500 μm (C) and 200
718 μm (D).
719 (E) Dot plots showing normalized ratio of mean fluorescence intensity of Alexa488-
720 CTb at Str (striatum). Sample size (*n*) denotes the number of images.
721
722 **Supplementary figure 4. Decreased SNr projection to thalamus in PDZD8$^{-/-}$ mice.**
723 Confocal and merged DIC images of thalamic regions showing SNr projection targets.
724 PalGFP signals in thalamus indicate SNr projections to the ventral anterior-lateral
725 complex of the thalamus (VAL) and ventromedial thalamus (VM). Scale bars, 200 μm.
726
727 **Supplementary table 1. Information of mouse age and sex.**
728 The age and sex of mice used in this study were summarized.
729
730 **Supplementary table 2. Information of neuronal tracer injection.**
731 Concentration, volume, target region, and coordinates from Bregma for Alexa594-CTb,
732 Alexa488-CTb, and AAV2/1-CMV-palGFP were summarized.
733
734 **Supplementary movie. 3D movies of lipid deposits in SNr in PDZD8$^{-/-}$ mice.**
735 (A, B) 3D movies of LipiDye II (green) and GFAP (magenta) in medial (A) and lateral
736 (B) regions of SNr in PDZD8$^{-/-}$ mice, which are corresponding to Figure 4B and C,
737 respectively. Scale bars, 10 μm.
738

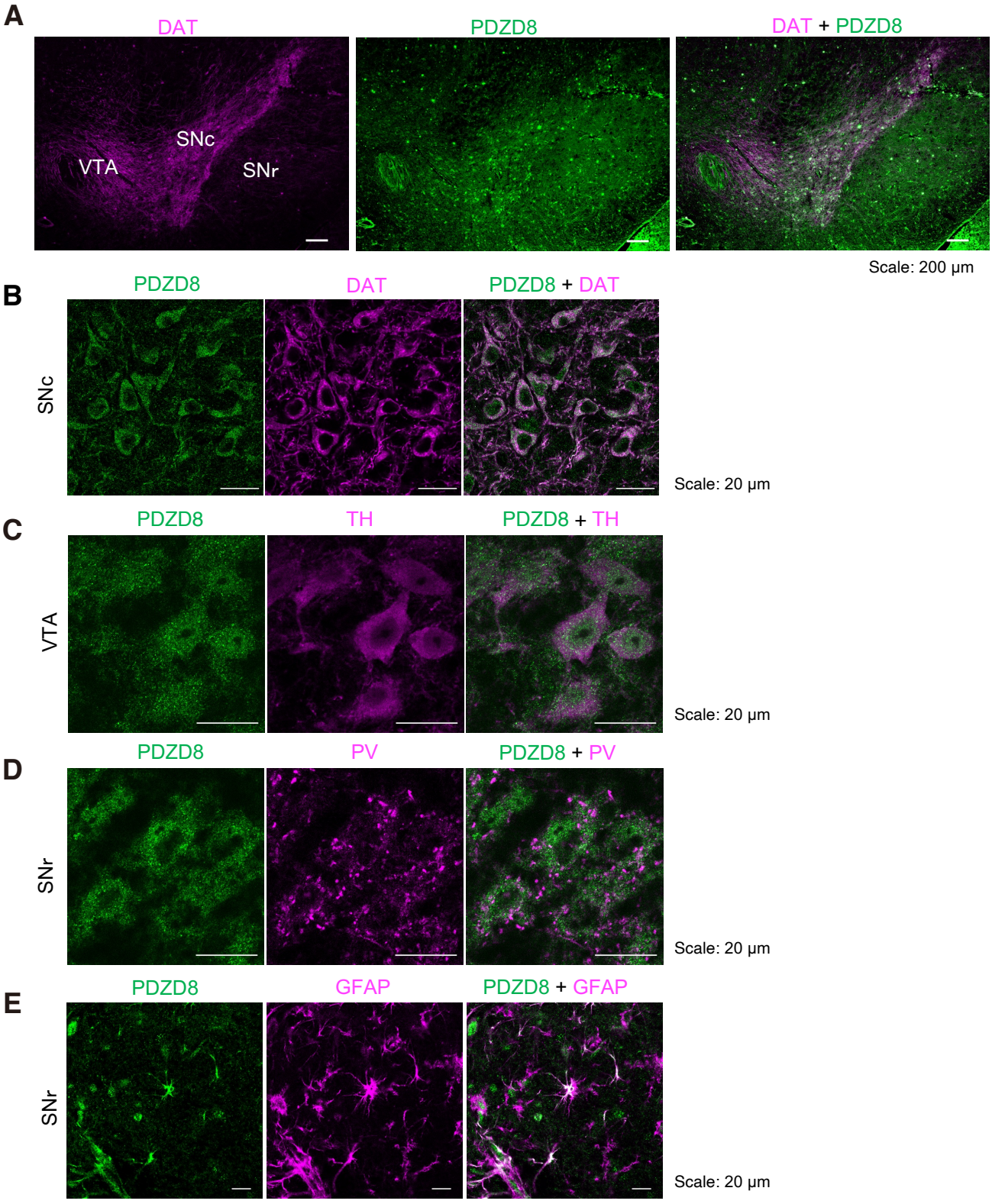
A
DAT
PDZD8
DAT + PDZD8
SNc
VTA
SNr
Scale: 200 μm
B
PDZD8
DAT
PDZD8 + DAT
SNc
Scale: 20 μm
C
PDZD8
TH
PDZD8 + TH
VTA
Scale: 20 μm
D
PDZD8
PV
PDZD8 + PV
SNr
Scale: 20 μm
E
PDZD8
GFAP
PDZD8 + GFAP
SNr
Scale: 20 μm

Figure 1

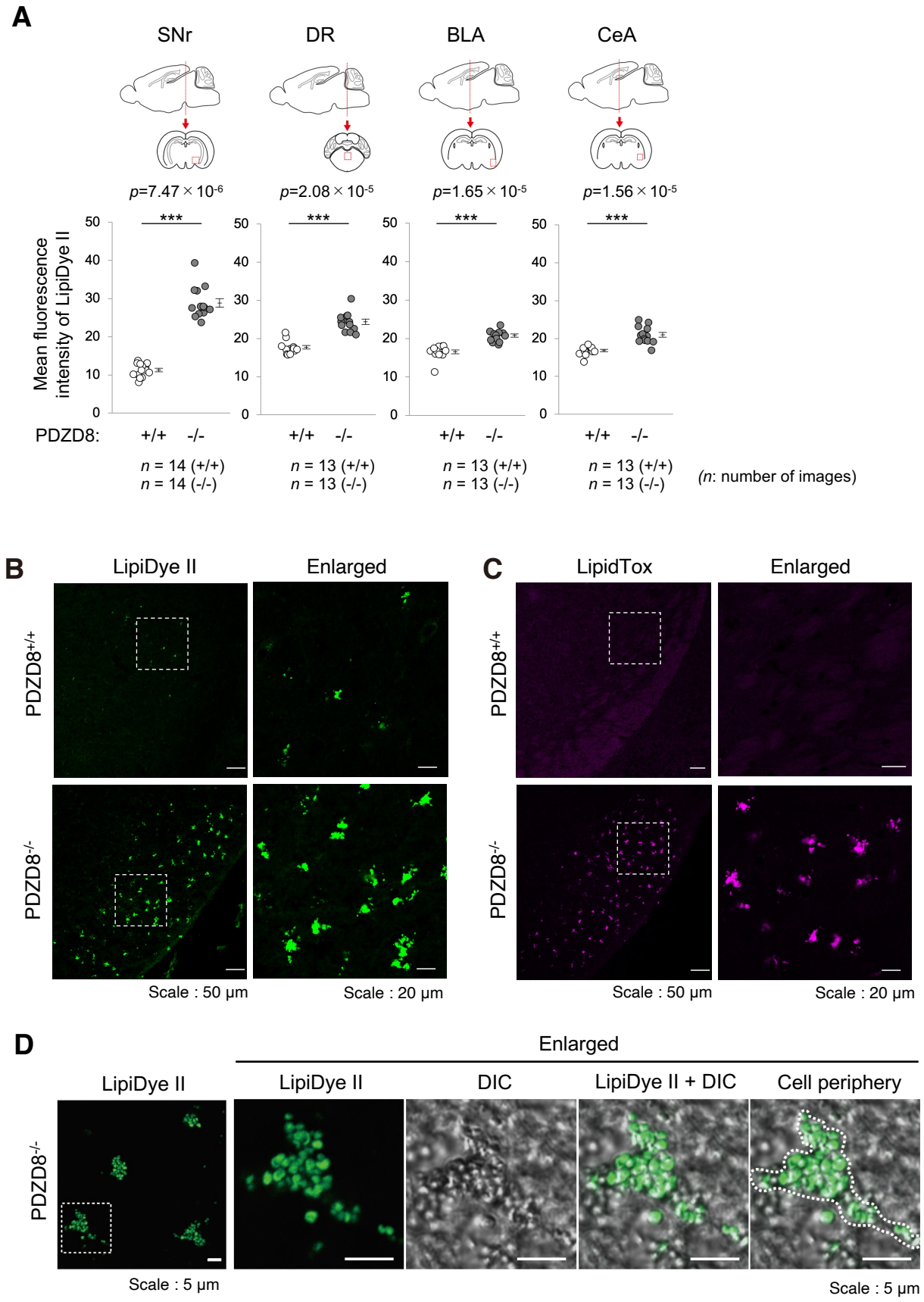
A
SNr
DR
BLA
CeA
p=7.47 × 10-6
p=2.08 × 10-5
p=1.65 × 10-5
p=1.56 × 10-5
***
Mean fluorescence intensity of LipiDye II
PDZD8:
+/+
-/-
n = 14 (+/+)
n = 14 (-/-)
n = 13 (+/+)
n = 13 (-/-)
(n: number of images)
B
LipiDye II
Enlarged
PDZD8+/+
PDZD8-/-
Scale : 50 μm
Scale : 20 μm
C
LipidTox
Enlarged
PDZD8+/+
PDZD8-/-
Scale : 50 μm
Scale : 20 μm
D
Enlarged
LipiDye II
LipiDye II
DIC
LipiDye II + DIC
Cell periphery
PDZD8-/-
Scale : 5 μm
Scale : 5 μm

Figure 2

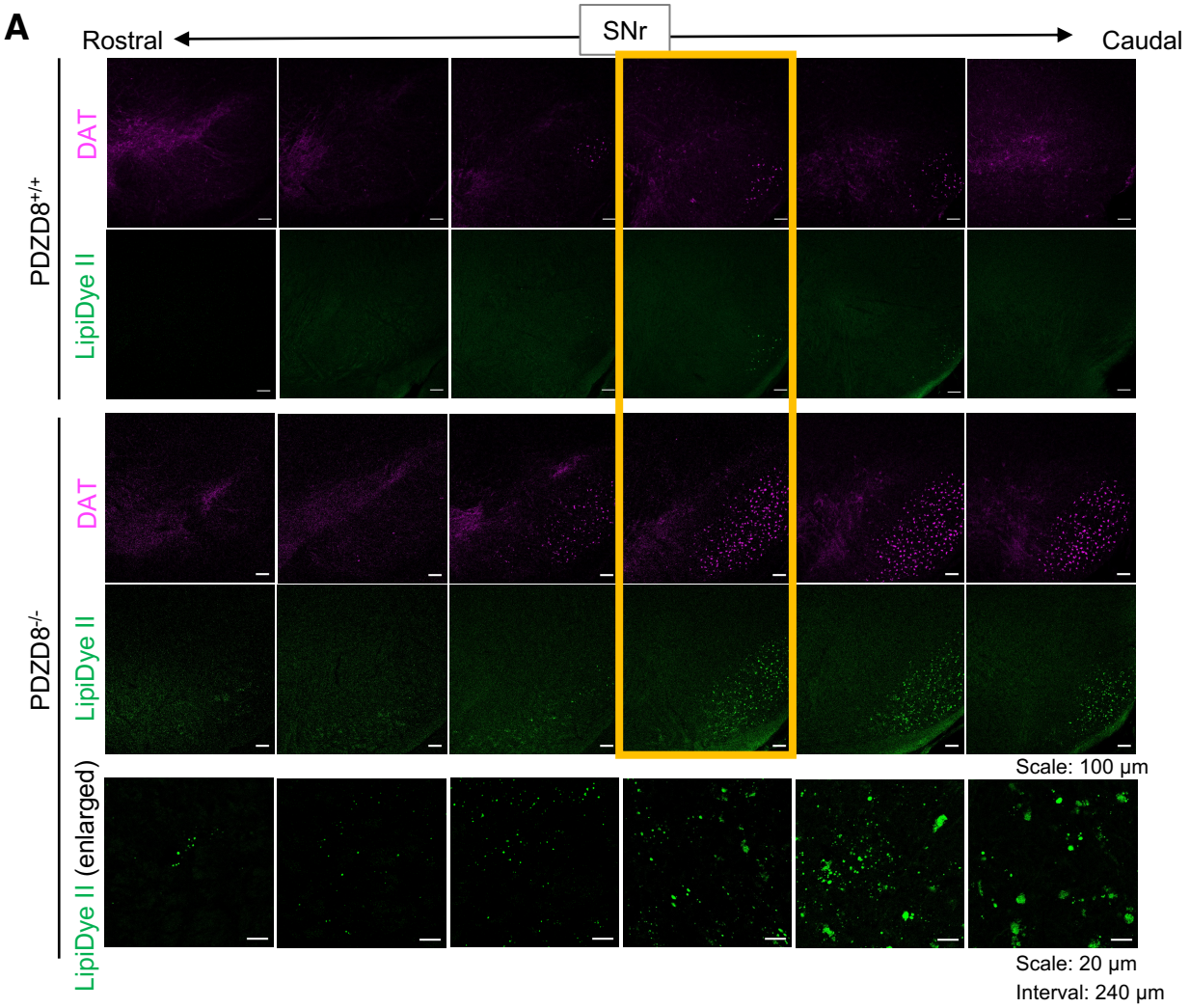
A
Rostral
SNr
Caudal
PDZD8+/+
DAT
LipiDye II
PDZD8-/-
DAT
LipiDye II
LipiDye II (enlarged)
Scale: 100 μm
Scale: 20 μm
Interval: 240 μm

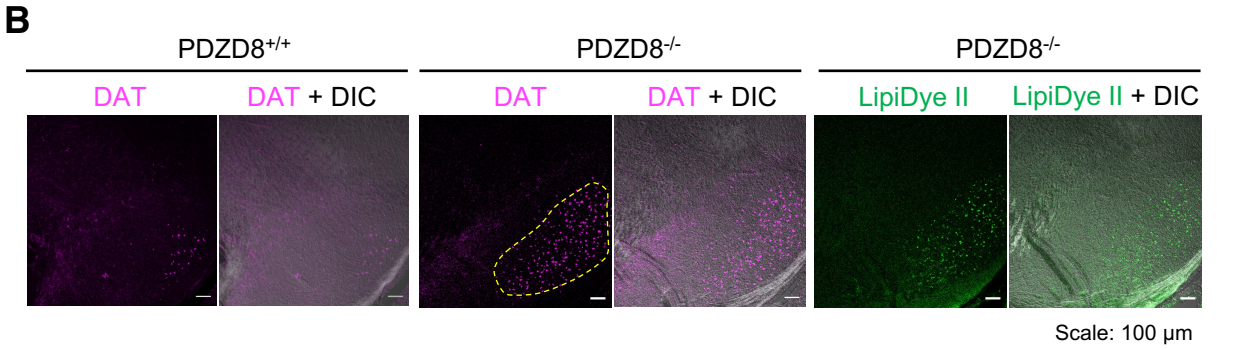
B
PDZD8+/+
PDZD8-/-
PDZD8-/-
DAT
DAT + DIC
DAT
DAT + DIC
LipiDye II
LipiDye II + DIC
Scale: 100 μm

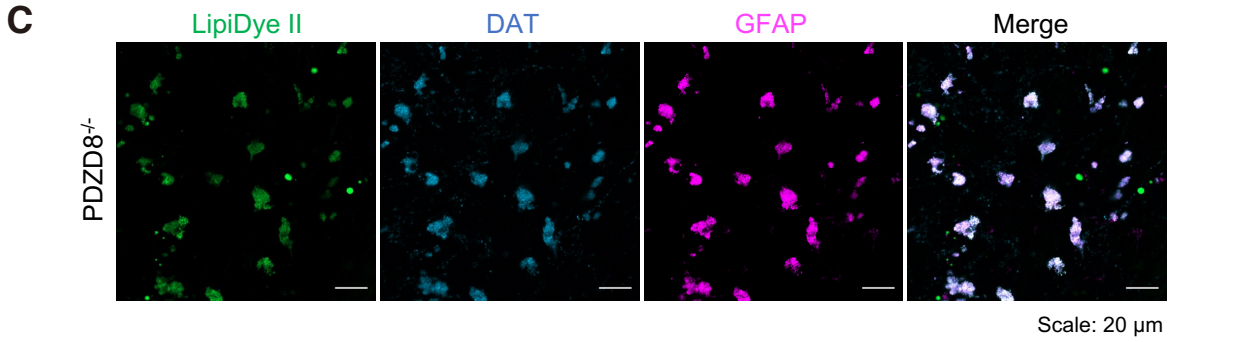
C
LipiDye II
DAT
GFAP
Merge
PDZD8-/-
Scale: 20 μm

Figure 3

A

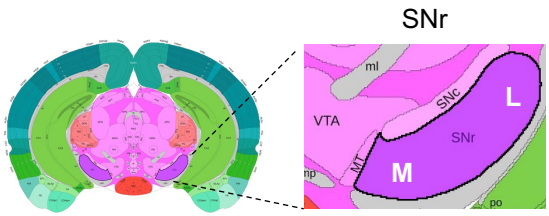

B

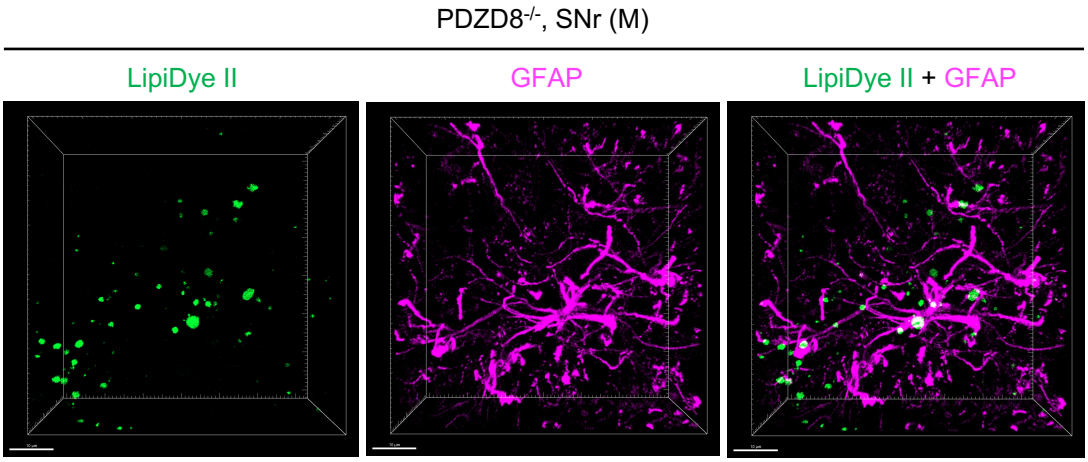

Scale: 10 μm

C

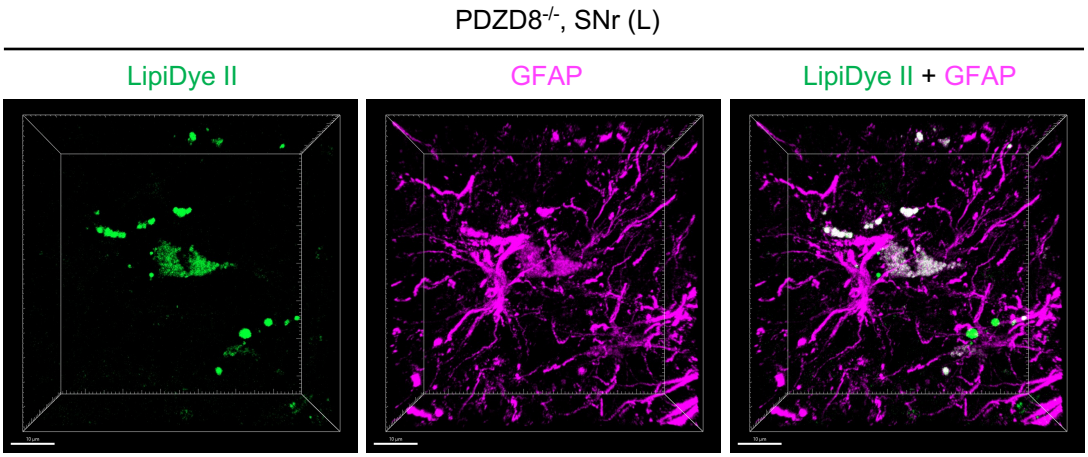

Scale: 10 μm

Figure 4

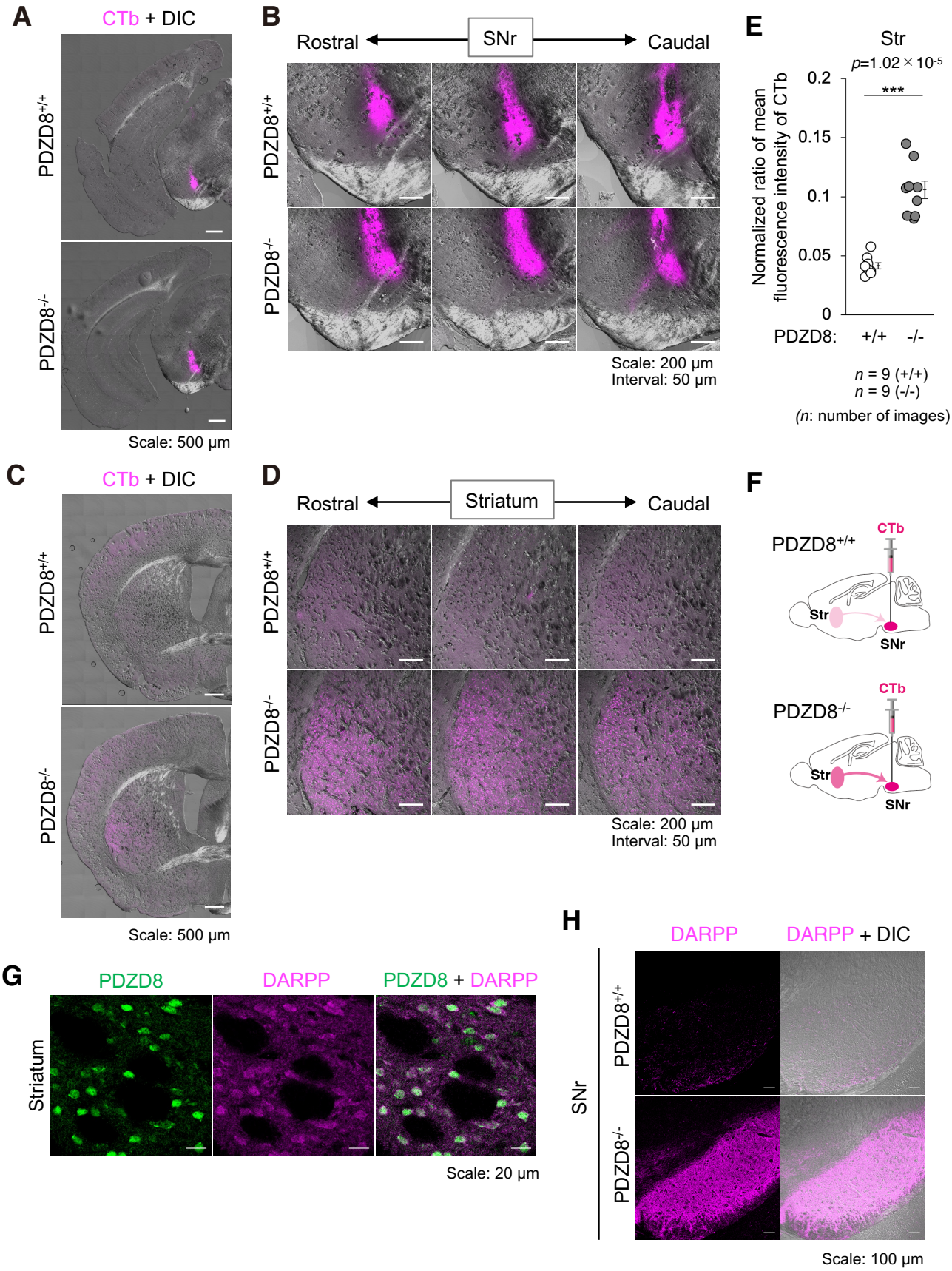
A
CTb + DIC
PDZD8+/+
PDZD8-/-
Scale: 500 μm
B
Rostral
SNr
Caudal
PDZD8+/+
PDZD8-/-
Scale: 200 μm
Interval: 50 μm
E
Str
p=1.02 × 10-5
***
Normalized ratio of mean fluorescence intensity of CTb
0.2
0.15
0.1
0.05
0
PDZD8: +/+ -/-
n = 9 (+/+)
n = 9 (-/-)
(n: number of images)
C
CTb + DIC
PDZD8+/+
PDZD8-/-
Scale: 500 μm
D
Rostral
Striatum
Caudal
PDZD8+/+
PDZD8-/-
Scale: 200 μm
Interval: 50 μm
F
PDZD8+/+
CTb
Str
SNr
PDZD8-/-
CTb
Str
SNr
G
PDZD8
DARPP
PDZD8 + DARPP
Striatum
Scale: 20 μm
H
DARPP
DARPP + DIC
SNr
PDZD8+/+
PDZD8-/-
Scale: 100 μm

Figure 5

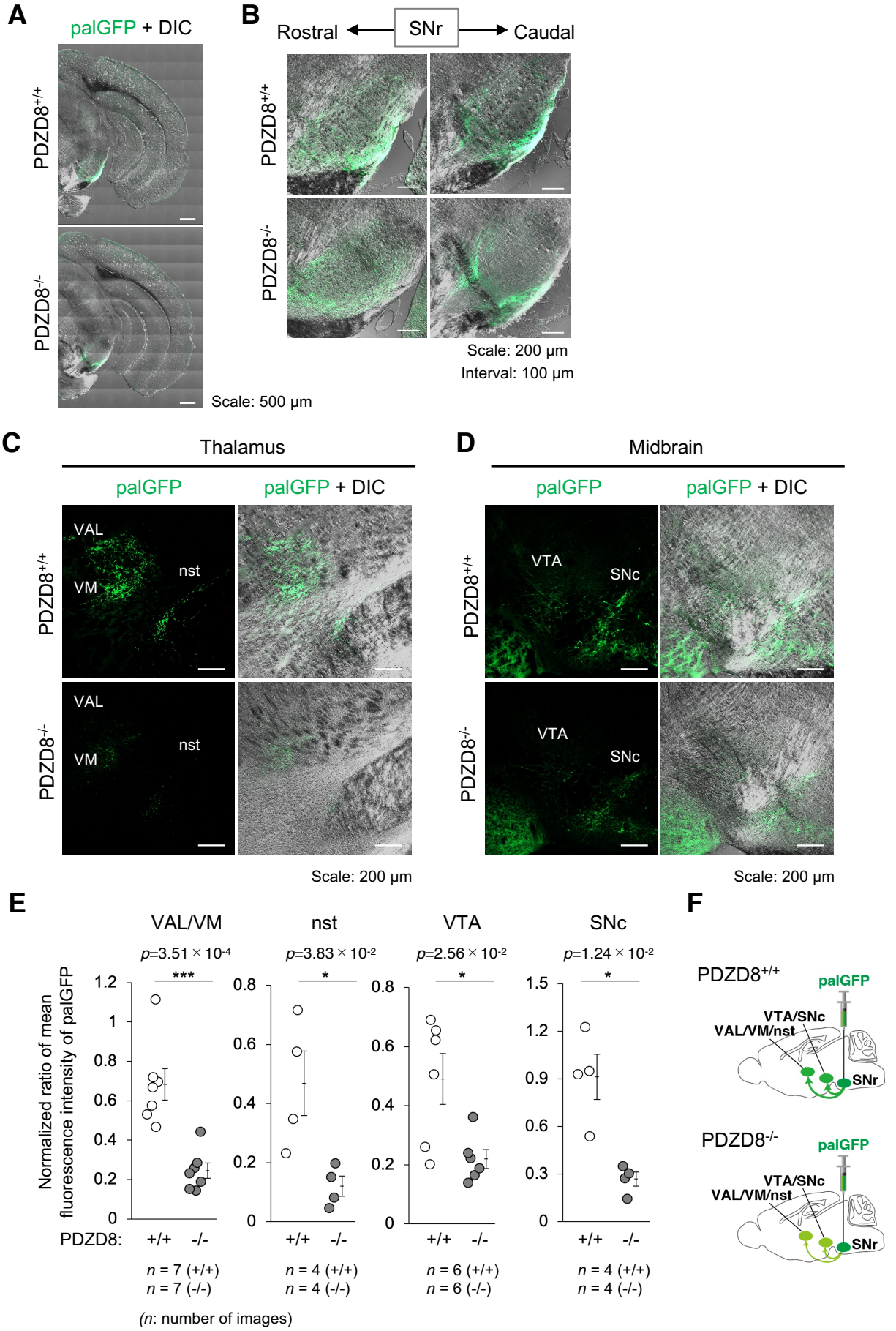
A
palGFP + DIC
PDZD8+/+
PDZD8-/-
Scale: 500 μm
B
Rostral
SNr
Caudal
PDZD8+/+
PDZD8-/-
Scale: 200 μm
Interval: 100 μm
C
Thalamus
palGFP
palGFP + DIC
VAL
VM
nst
PDZD8+/+
PDZD8-/-
Scale: 200 μm
D
Midbrain
palGFP
palGFP + DIC
VTA
SNc
PDZD8+/+
PDZD8-/-
Scale: 200 μm
E
VAL/VM
nst
VTA
SNc
p=3.51 × 10-4
p=3.83 × 10-2
p=2.56 × 10-2
p=1.24 × 10-2
***
*
*
*
Normalized ratio of mean fluorescence intensity of palGFP
PDZD8: +/+ -/-
n = 7 (+/+)
n = 7 (-/-)
n = 4 (+/+)
n = 4 (-/-)
n = 6 (+/+)
n = 6 (-/-)
n = 4 (+/+)
n = 4 (-/-)
(n: number of images)
F
PDZD8+/+
palGFP
VTA/SNc
VAL/VM/nst
SNr
PDZD8-/-
palGFP
VTA/SNc
VAL/VM/nst
SNr

Figure 6

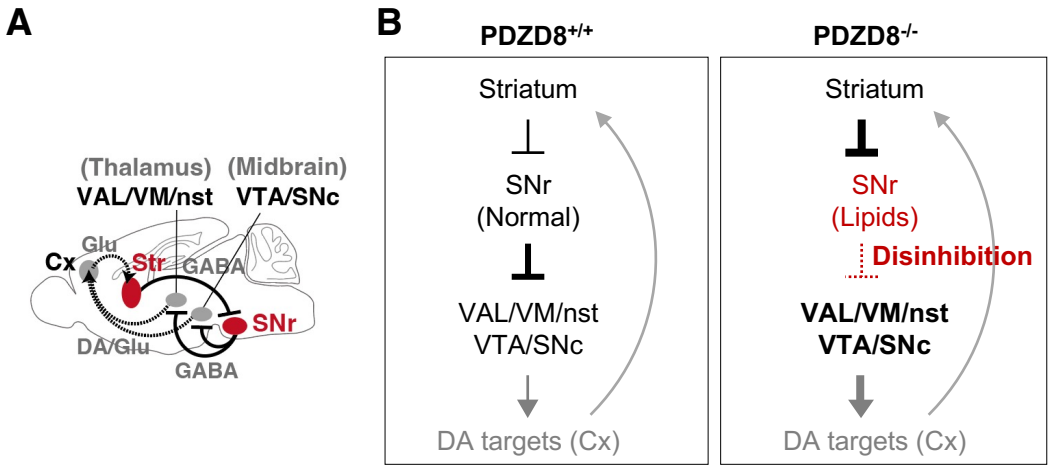
A
(Thalamus)
VAL/VM/nst
(Midbrain)
VTA/SNc
Glu
Cx
Str
GABA
SNr
DA/Glu
GABA
B
PDZD8+/+
Striatum
SNr
(Normal)
VAL/VM/nst
VTA/SNc
DA targets (Cx)
PDZD8-/-
Striatum
SNr
(Lipids)
Disinhibition
VAL/VM/nst
VTA/SNc
DA targets (Cx)

Figure 7